33rd Symposium on Naval Hydrodynamics
Osaka, Japan, 18 Oct-23 Oct 2020

Direct numerical simulation of realistic rough surfaces and energy minimization for the prediction of interfacial equilibrium position

R. Ma[1], K. Alamé[1], S. Anantharamu[1] and K. Mahesh[1]
([1]Department of Aerospace Engineering and Mechanics, University of Minnesota, USA

ABSTRACT

Direct numerical simulation (DNS) is performed for a turbulent channel flow at $Re_\tau = 400$. A realistic rough surface, corresponding to the experiments of Flack et al. (2019) is used on the bottom wall, while the top wall is smooth. The skin-friction coefficient matches the experimental results of Flack et al. (2019) for the same rough surface. A double-averaging methodology is used to investigate the roughness effects on the mean flow, including the double-averaged flow field in the rough layer, dispersive stresses compared to Reynolds stresses, and pressure fluctuations. It is found that the magnitude of dispersive stresses is smaller than that of Reynolds stresses. The pressure fluctuations are enhanced in the near-wall region, due to the peaky structures of the roughness elements. The investigation of the dominant mean-shear and turbulence-turbulence source terms of the Poisson's equation suggest that the shear layer induced by roughness protrusions, the streamwise vortices and secondary flow interactions among the roughness elements contribute to the increased pressure fluctuations in the rough-wall flows. For the smooth wall case, we analyze the sources of wall-pressure fluctuations using a novel framework that combines the DNS data, Green's function formulation and spectral Proper Orthogonal Decomposition (POD). The sources responsible for the premultiplied peak in the power spectra at $\omega^+ \approx 0.35$ peak in the buffer region for $Re_\tau = 180$ and 400. Spectral POD supports the case that the wall-pressure fluctuation sources can be classified into two decorrelated parts - active and inactive. We further investigate the active component of the source by examining the obtained spectral POD modes. To analyze the effectiveness of the rough surface to sustain an interface, we use a recently developed level set methodology based on energy minimization. The algorithm gives equilibrium interface shapes over a wide variety of rough surfaces for different static pressures. The method is applied to user defined roughness and realistic roughness obtained from surface scans.

INTRODUCTION

Surface roughness plays an important role in the operation and performance of fluidic engineering devices. Realistic rough surfaces are being studied in recent years both experimentally and computationally. Compared to the regular roughness patterns, the turbulence effects are more complex and less understood for realistic surfaces.

Jiménez (2004) summarised roughness effects on turbulent flows and highlighted that when the roughness scales are sufficiently small, the effects are limited to a near-wall layer, i.e. roughness sublayer, while the turbulent statistics of the outer layer remain the same as smooth-wall flows. Since three-dimensional rough surfaces can produce inhomogeneous flow fields in the roughness sublayer, the double-averaging decomposition is applied to investigate the spatial heterogeneity in time-averaged flow variables. This methodology was introduced by Raupach and Shaw (1982) to examine the "wake production" term within vegetation canopies. Many studies on regular rough surfaces have investigated dispersive stresses. Cheng and Castro (2002) conducted measurements over urban roughness and found that the dispersive stresses in the roughness sublayer are negligible compared to the spatially averaged Reynolds stresses. Coceal et al. (2007) used DNS to investigate the spatial heterogeneity within regular cube arrays and found that the dispersive stress is mostly concentrated in the wake regions. Studies in the context of irregular rough surfaces were carried out recently to investigate double-averaged (DA) statistics. A numerical study was conducted by Forooghi et al. (2018) for turbulent channel flows over random roughness with high slopes to investigate the effects of surface statistics on the

Reynolds and dispersive stresses. Yuan and Jouybari (2018) performed DNS to contrast two realistic surfaces with different range of scales in terms of the momentum transfer and energy production. Jelly and Busse (2019) provided a detailed analysis on the Reynolds number dependence of Reynolds and dispersive stresses for irregular near-Gaussian roughness.

The wall-pressure fluctuations are of importance for both smooth and rough walls. They excite flexible structures thereby resulting in far-field sound radiation. Also, the pressure fluctuations are a global quantity because it satisfies a Poisson equation. Thus arguments that are based on local length and velocity scales that have worked reasonably well for velocity, might not work very well to analyze pressure fluctuations. We will sometimes refer wall-pressure fluctuations as just wall-pressure for brevity.

We now discuss some previous works on analyzing sources of smooth wall-pressure fluctuations in wall-bounded flows. Farabee and Casarella (1991) measured the power spectral density (PSD) of wall-pressure under a turbulent boundary layer for different freestream velocities. They used scaling arguments to decipher the location of sources of wall-pressure for different frequency ranges. Based on the collapse of the PSD, they hypothesized that the dominant contribution to the low ($\omega\delta/u_\tau < 5$), mid ($5 < \omega\delta/u_\tau < 100$) and high frequency regions ($\omega\delta/u_\tau > 0.3Re_\tau$) of the wall-pressure PSD to be from the unsteady potential region (above the boundary layer), outer region and inner region of the boundary layer, respectively. Chang III et al. (1999) analyzed the contribution of sources in viscous, buffer, logarithmic and outer region to wall-pressure wavenumber spectra by computing partial pressures. Overall, they found that the buffer region is the dominant source of wall-pressures for both low and high wavenumbers. Panton et al. (2017) studied wall-pressure using turbulent channel flow DNS data at Re_τ ranging from $180-5200$. The premultiplied wall-pressure streamwise wavenumber spectra showed a peak around $\lambda_1^+ \approx 200-300$ for all Re_τ. For $Re_\tau > 1000$, Panton et al. (2017) observed a non-negligible contribution from the low-wavenumber range to the RMS wall-pressure. This contribution grew and separated from the high wavenumber peak at λ_l^+ with increasing Reynolds numbers. Since, the low wavenumber peak did not scale in inner units, the sources responsible for this peak were believed to be in the outer region.

Realistic rough surfaces are also of great interest to the superhydrophobic community due to their impact on skin friction and pressure drag which can modify near-wall flow structures in turbulent flows. The wetted condition is known as the Wenzel state (Wenzel, 1936). The ability for the roughness to entrap gas within the microtexture when submerged in water is known as the Cassie-Baxter state (Cassie and Baxter, 1944). This is relevant to superhydrophobicity and wall nucleation due to its impact on drag reduction and cavitation. The multiphase aspect of the simulations is to examine the distribution of the liquid-gas interface over a realistic rough surface which is difficult to measure experimentally. Bottiglione and Carbone (2012) investigated the effect of statistical properties of the surface roughness using an analytical approach to minimize the Gibbs free energy of a liquid-air interface over a 1D roughness; an extension to a higher dimension was not examined. Alamé et al. (2019) proposed a level set methodology without reinitialization based on energy minimization to obtain the liquid-gas interface over arbitrary realistic roughness at equilibrium.

In this paper, we perform DNS of turbulent channel flow over realistic surfaces and explore the roughness effects on the mean flow and turbulent statistics using the double-averaging decomposition. We investigate the pressure fluctuations in rough-wall flows and take the first steps towards examining the role of Poisson's equation contributors to the pressure fluctuations in the roughness sublayer. For smooth walls, we discuss a novel framework (Anantharamu and Mahesh, 2020) to analyze sources of wall-pressure fluctuations at $Re_\tau = 180$ and 400. The methodology combines Direct Numerical Simulation (DNS) data, Green's function formulation and spectral POD. We are currently extending the framework to analyze sources of rough-wall wall-pressure fluctuations. Finally, using Gibbs free energy minimization, we investigate the effect of external pressure on the liquid-air interface equilibrium location over a wide variety of surfaces.

SIMULATION DETAILS

The governing equations are solved using the finite volume algorithm developed by Mahesh et al. (2004) for the incompressible Navier-Stokes equations. The governing equations for the momentum and continuity equations are given by the Navier-Stokes equations:

$$\frac{\partial u_i}{\partial t} + \frac{\partial}{\partial x_j}(u_i u_j) = -\frac{\partial p}{\partial x_i} + \nu \frac{\partial^2 u_i}{\partial x_i x_j} + K_i, \qquad (1)$$

$$\frac{\partial u_i}{\partial x_i} = 0, \qquad (2)$$

where u_i and x_i are the i-th (1-streamwise, 2-wall-normal, 3-spanwise) component of the velocity and position vectors respectively, p denotes pressure, ν is the kinematic viscosity of the fluid and K_i is a constant pressure gradient (divided by density). The algorithm is robust and emphasizes discrete kinetic energy

conservation in the inviscid limit. This enables simulation of high-Re flows without adding numerical dissipation. A predictor-corrector methodology is used where the velocities are first predicted using the momentum equation, and then corrected using the pressure gradient obtained from the Poisson equation yielded by the continuity equation. The Poisson equation is solved using a multigrid pre-conditioned conjugate gradient method (CGM) using the Trilinos libraries (Sandia National Labs). The Crank-Nicholson discretization with a linearization of the convective terms and a successive over relaxation (SOR) method is used for implicit time advancement.

The surface is represented by obstacle cells which are masked out. We ensure that the p.d.fs, statistics, and spectra of the masked surface agree acceptably with the experimental scan (Ma et al., 2021). The wetted masked cells (cells that share a face between a fluid and obstacle cell) enforce a zero face-normal velocity. No-slip Dirichlet boundary conditions are enforced on the face velocities of the rough surface in the computations.

In the context of the Gibbs free energy minimization, a different approach is taken. Instead of solving the Navier-Stokes equations, we begin by defining a total energy of the system $\mathscr{E}(\phi) = \mathscr{E}_{\mathscr{B}}(\phi) + \mathscr{E}_{\mathscr{I}}(\phi) + \mathscr{R}_p(\phi)$ that is the sum of the bulk energy $\mathscr{E}_{\mathscr{B}}(\phi)$ (due to an external pressure), surface energy $\mathscr{E}_{\mathscr{I}}(\phi)$ (due to surface tension) and $\mathscr{R}_p(\phi)$ the penalty function that keeps the level set a signed distance function. By taking the Fréchet derivative of the energy functional, we obtain a steepest descent minimization in the form of a level set advection-diffusion equation given by:

$$\frac{\partial \phi(\mathbf{x},t)}{\partial t} = \alpha \nabla \cdot \left(d_p\big(|\nabla \phi(\mathbf{x},t)|\big) \nabla \phi(\mathbf{x},t) \right) + \delta\big(\phi(\mathbf{x},t)\big) \left[\nabla \cdot \left(\tau(\mathbf{x}) \frac{\nabla \phi(\mathbf{x},t)}{|\nabla \phi(\mathbf{x},t)|} \right) + \Delta p H(-\psi(\mathbf{x})) + \mu H(\psi(\mathbf{x})) \right]. \quad (3)$$

The signed distance functions (SDF) $\phi(\mathbf{x})$ and $\psi(\mathbf{x})$ are level sets that track the two fluids and the solid surface respectively. $\phi(\mathbf{x}) > 0$ in the liquid region, $\phi(\mathbf{x}) < 0$ in the air region, and $\phi(\mathbf{x}) = 0$ at the liquid-air interface. Similarly for $\psi(\mathbf{x})$ which denotes the solid region. $H(\cdot)$ is the Heaviside function and $\delta(\cdot)$ is the Dirac delta function. The first term on the right hand side is the level set regularization term which enforces the level set to remain an SDF ; this removes the need to reinitialize every time-step. The premultiplier α is a weighting coefficient for regularization. The second term is the surface tension-curvature product where $\tau(\mathbf{x})$ is the surface tension and $\nabla \cdot \left(\frac{\nabla \phi(\mathbf{x},t)}{|\nabla \phi(\mathbf{x},t)|} \right)$ is the curvature κ. The third term Δp is the external pressure which is only active outside the solid region. The Lagrange multiplier μ satisfies the no-penetration constraint (i.e. the interface level set $\phi(\mathbf{x})$ does not intersect and penetrate the solid level set $\psi(\mathbf{x})$). At equilibrium, the surface tension term balances with the pressure term. This results in the Young-Laplace equation $\Delta p = \tau\kappa$, while the other terms go to zero. Further details into the numerical implementation of the method and how the Lagrange multipliers are computed can be found in Alamé et al. (2019).

COMPUTATIONAL SETUP

Surface generation

The rough surface is processed from the experimental scans provided by Flack and Schultz (personal communication). Each tile is a rectangular patch of roughness with $k_{rms} \approx 88\mu m$, which is interpolated into the grids size based on the streamwise and spanwise resolution in the simulation. Several rough tiles are then tiled in random rotations to minimize the directional bias and achieve a larger domain size. The simulation domain size of $2\pi\delta \times \pi\delta$, where δ is the channel half-height, is then extracted from the tiled surface. The length, width of the rough surface and the roughness height are all scaled by δ.

At the beginning of a simulation run, the values of the roughness height are read and interpolated to the cell centres. Any obstacle cell which shares an edge with a fluid cell is tagged as a boundary cell. Boundary cells can either be an edge cell (if the boundary cell borders exactly one fluid cell) or a corner cell (if the boundary cell shares a corner with two or more fluid cells). The momentum equations are solved inside the fluid domain while the pressure is solved in both fluid and solid domains. No-slip boundary conditions are applied at the edge cells and a weighted average of the neighbouring cells is applied at the corners. This does not affect the pressure equation since we use collocated grids where the face-normal velocities are set to zero at the boundaries independent of the cell centre value. This ensures a proper pressure jump recovery at the obstacle walls.

The surface statistics of the rough surface before scaling are shown in table 1. Figure 1 visualises the rough surface. Figure 2 shows a direct comparison of a cross section of the surface profile between the original experimental scan and the processed surface. Note that the small scales are smoothed out but the profile remains a reasonable approximation.

Table 1: Surface statistics of the processed realistic rough surface

Parameter	Description	k/δ	k^+
k_a	Average Roughness Height	0.006	2.4
k_{rms}	RMS Roughness Height	0.007	2.8
k_t	Maximum Peak to Valley Height	0.06	24
Sk	Skewness	-0.053	
Ku	Kurtosis	2.933	
ES_x	Effective Slope of Roughness in x	0.265	
ES_z	Effective Slope of Roughness in z	0.265	

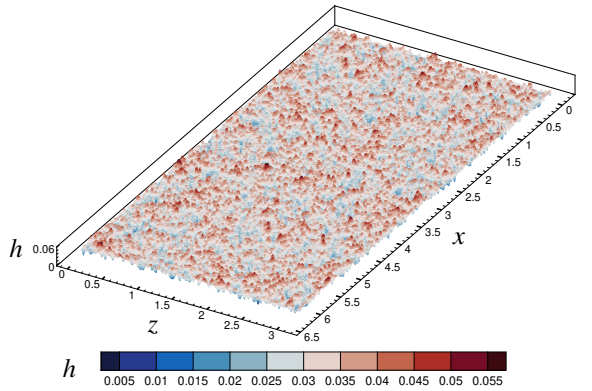

Figure 1: Illustration of the rough surface. The contour legend describes the height of the surface profile normalized by δ.

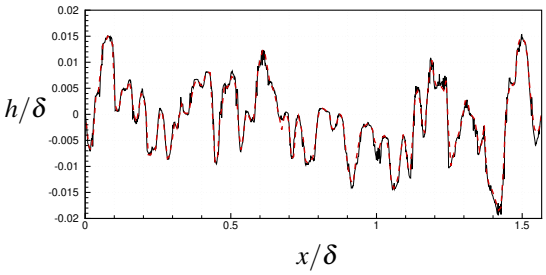

Figure 2: Comparison of a cross section of the computational surface to the experimental scan. The solid black line shows the experimental surface, and the dashed red line shows the computational rough surface for Case $k_{rms} \approx 88\mu m$.

Problem description

Simulations are performed for a turbulent channel flow at $Re_\tau = u_\tau \delta/\nu = 400$, where the rough surface is applied on the bottom wall only. A smooth turbulent channel flow at the same Re_τ is performed for comparison. No-slip boundary conditions are used on both the top and bottom walls with periodicity in the streamwise (x) and spanwise (z) directions. Non-uniform grids are used in the wall-normal (y) direction with grids clustering near the surface region. k_s^+ is equal to 6.4 for the rough case. The case names, domains and grid details are shown in table 2 and 3. For further information of the rough surface, the validations of our flow solver and the grid convergence study, we refer the reader to Ma et al. (2021). The streamwise, spanwise, and wall-normal resolutions adhere to the criteria suggested by Busse et al. (2015). The smallest roughness feature, estimated by the smallest wavelength λ_{min}, is resolved by 14 grid points.

Table 2: Domains and meshes of simulation cases.

Case	$L_x \times L_y \times L_z$	$N_x \times N_y \times N_z$
Smooth	$2\pi\delta \times 2\delta \times \pi\delta$	$768 \times 320 \times 384$
$k_{rms} \approx 88\mu m$	$2\pi\delta \times 2.03\delta \times \pi\delta$	$768 \times 320 \times 384$

Table 3: Grid resolution of simulation cases.

Case	Δx^+	Δz^+	Δy^+_{min}	Δy^+_{max}	$\lambda_{min}/\Delta x$
Smooth	3.27	3.27	0.85	5.48	-
$k_{rms} \approx 88\mu m$	3.27	3.27	0.85	5.64	14

A constant pressure gradient is set to drive the channel flow, thus the average friction velocity u_τ is given by $u_\tau = (\delta K_1)^{1/2}$. For Case $k_{rms} \approx 88\mu m$, since the top wall is smooth and the bottom wall is rough, the shear stress over the smooth wall, τ_w^t, is calculated by averaging $\mu(\partial\overline{u}/\partial y)|_{y=L_y}$ over the wall. The rough-wall shear stress τ_w^b is then computed from the force balance between the drag of the walls and the driven force. The bottom wall friction velocity is then calculated by $u_\tau^b = (\tau_w^b/\rho)^{1/2}$.

Double-averaging methodology

Since the roughness leads to spatial heterogeneity of the time-averaged variables, the double-averaging decomposition (Raupach and Shaw (1982)) is applied to separate the spatial variation in the homogeneous and non-homogeneous directions from the time-averaged quantities,

$$\theta(x,y,z,t) = \langle\overline{\theta}\rangle(y) + \tilde{\theta}(x,y,z) + \theta'(x,y,z,t). \quad (4)$$

θ represents any instantaneous flow variable. $\overline{\theta}$ is the time-averaged variable. The instantaneous turbulent fluctuation θ' is thus obtained by extracting the temporal

average from the instantaneous variable, i.e. $\theta' = \theta - \overline{\theta}$. The bracket is the spatial-averaging operator,

$$\langle\overline{\theta}\rangle(y) = 1/A_f \int\int_{A_f} \overline{\theta}(x,y,z)dxdz, \tag{5}$$

where A_f is the fluid-occupied area. The form-induced dispersive component, $\tilde{\theta}$, is defined as $\tilde{\theta} = \overline{\theta} - \langle\overline{\theta}\rangle$, which presents the spatial variation of the time-averaged flow variables.

According to the decomposition in equation 4, the Reynolds stress tensor is defined as

$$\overline{u_i'u_j'} = \overline{(u_i - \overline{u_i})(u_j - \overline{u_j})}, \tag{6}$$

and the dispersive stress tensor is defined as

$$\tilde{u_i}\tilde{u_j} = (\overline{u_i} - \langle\overline{u_i}\rangle)(\overline{u_j} - \langle\overline{u_j}\rangle). \tag{7}$$

Surface scans as a solid boundary for Gibbs energy minimization

In order to represent the surface in the Gibbs energy minimization, the solid has to be defined as a continuous implicit function (i.e. a level set). The original algorithm presented in Alamé et al. (2019) relied on a user defined input where the solid level set is known a priori and is supplied as an initial condition. Here the algorithm is extended such that a level set can be reconstructed from a point cloud data of a real surface scan without any knowledge of its surface properties (e.g. surface normals), all that is needed is a height distribution over the streamwise and spanwise dimensions. This is done in a 3 step process after reading in the height map:

1. Reconstruct a signed distance field from the point cloud data, this is done by solving the Eikonal equation $|\nabla d(x)|$ where $d(x)$ is the distance function. A Gauss-Seidel iterative method is used.

2. Initialize a level set for the solid at an offset from $d(x)$, then solve a minimization problem between the gradient of the distance field and the gradient of the level set. This is given by $\phi_t = \delta(\phi)(\nabla d \cdot \nabla\phi)$. This leads to a level set reconstruction of the roughness.

3. Use the generated level set from the previous step as be read by the Gibbs free energy minimizer algorithm that initializes the above level set to a solid interface.

The surface data used is obtained from a real surface manufactured at UT Dallas (courtesy Professor Wonjae Choi), with a 3D surface profile measurement using a $50X$ objective lens obtained from MIT (courtesy Professor Gareth McKinley). The sample is made of aluminum 6061 sandblasted using 150 grit, etched for 25 seconds, boehmetized for 30 minutes, and hydrophobised using Ultra Ever Dry top coat in isopropanol. Figure 3 shows three different reconstructions with varying grid resolutions, $N_x \times N_y \times N_z = 128 \times 26 \times 128$, $256 \times 52 \times 256$, and $512 \times 106 \times 512$ respectively.

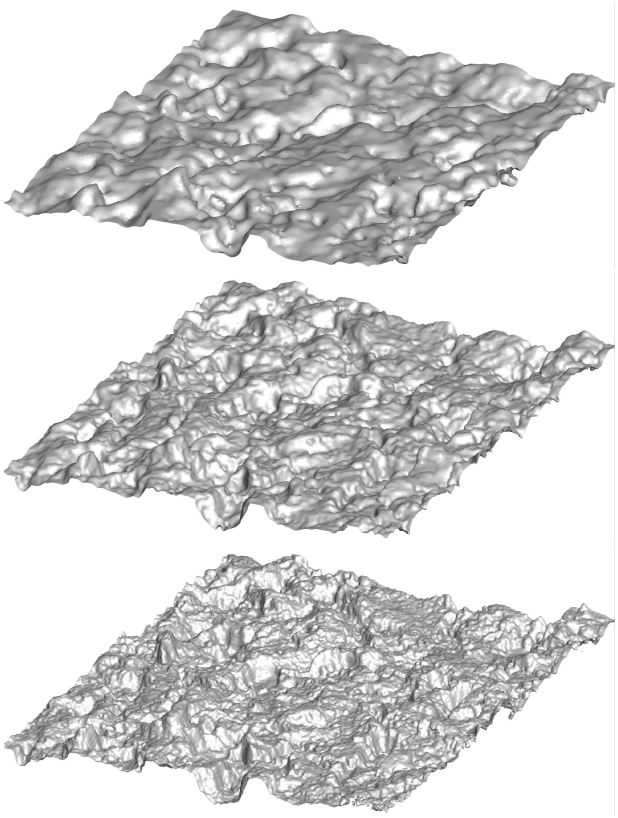

Figure 3: Real surface scanned data reconstructed as a level set for three different resolutions ranging from coarse, medium to a fine grid. Note the level of detail the reconstruction if able to provide.

The reconstruction algorithm is able to capture the smallest variations in the roughness, providing a powerful tool to reconstruct realistic surfaces for the energy minimization algorithm.

RESULTS AND DISCUSSION

Skin-friction coefficient

The skin-friction coefficient $C_f = \tau_w^b/(\frac{1}{2}\rho U_b^2)$ is computed, where U_b is the bulk velocity of the channel flow. The C_f value of Case $k_{rms} \approx 88\mu m$ is 0.00734, while the C_f from the experimental results of Flack et al. (2019) is 0.00740. The error of the simulation relative to experiment is 0.8%, which constitutes reasonable agreement.

DA statistics

The DA velocity of Case $k_{rms} \approx 88\mu m$ is presented in the inner coordinate, and compared to the smooth case in figure 4. The velocity is normalized by u_τ^b in the rough case and u_τ in the smooth case. The wall-normal distance y^+ in the rough case is equal to $(y-y_0)u_\tau^b/\nu$, where y_0 is the virtual origin, taken to be the arithmetic mean elevation of the rough surface. The rough case shows a slip velocity at the wall and a velocity deficit in the viscous wall region. The inset shows the profile in semi-log coordinate. The dotted line shows the peak location of the rough surface, corresponding to $y^+ = 12$. In the rough region ($y^+ \leq 12$), the velocity profile shows a gradual increase due to the drag effects of roughness. As y^+ extends beyond the rough region, the velocity displays a more constant offset from the smooth-wall profile and conforms to the log-law in the log-law region.

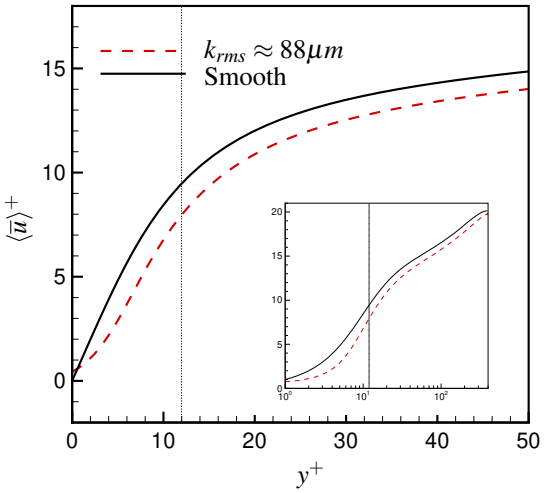

Figure 4: Mean velocity against wall-normal distance in the inner coordinate. The inset is shown on a semi-log scale.

To investigate the spatial variation of the time-averaged flow field in the rough region, the form-induced velocity field at $y^+ = 3$ is examined. Figure 5(a) shows that large positive and negative $\tilde{u}$ occurs in the large trough region between the roughness asperities, and the wake region behind the roughness elements, respectively. The distribution of $\tilde{v}$ in figure 5(b) is more sparse compared to $\tilde{u}$, but the high-magnitude positive $\tilde{v}$ occurs mostly in front of the roughness. Looking into the same region of the distribution of $\tilde{w}$ in figure 5(c), the pairs of the high magnitude of positive $\tilde{w}$ (red region) and negative $\tilde{w}$ (blue region) are observed in front of the roughness crests. This correlation indicates that the impulsive upward velocity produces the pairs of streamwise vortices. This has been suggested by Muppidi and Mahesh (2012) in their investigation of a regular rough-wall boundary layer. Here, we observe the same feature. However, unlike the regular rough wall case, the distribution and strength of the streamwise vortices depend on the irregular roughness geometry.

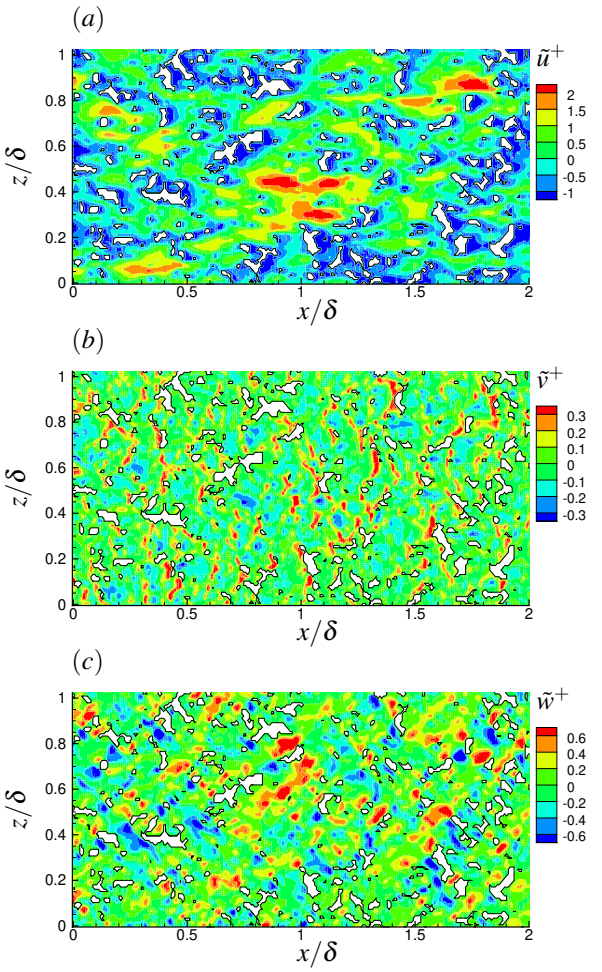

Figure 5: Form-induced velocity (a) $\tilde{u}^+$, (b) $\tilde{v}^+$, and (c) $\tilde{w}^+$ at $y^+ = 3$.

The pressure perturbation at the same y^+ location is shown in figure 6. Large positive $\tilde{p}$ (red region) is found to occur in front of the roughness asperities, while large negative $\tilde{p}$ (blue region) occurs behind the rough elements. The form drag is computed in two regions separately: one is the 'peak' region above the mean roughness height, the other is the 'valley' region below the mean height. The results show that the form drag in the 'peak' region contributes 73.8% of the total form drag. This suggests that the peaky structures of the rough surface contribute a large percentage of the form drag.

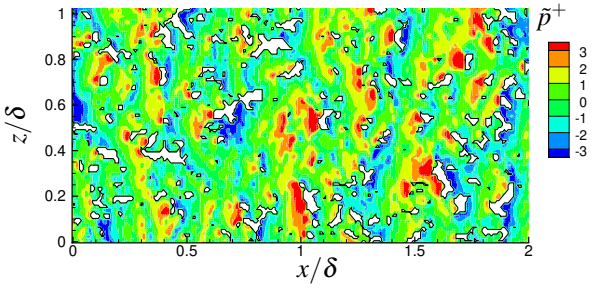

Figure 6: Form-induced pressure $\tilde{p}^+$ at $y^+ = 3$.

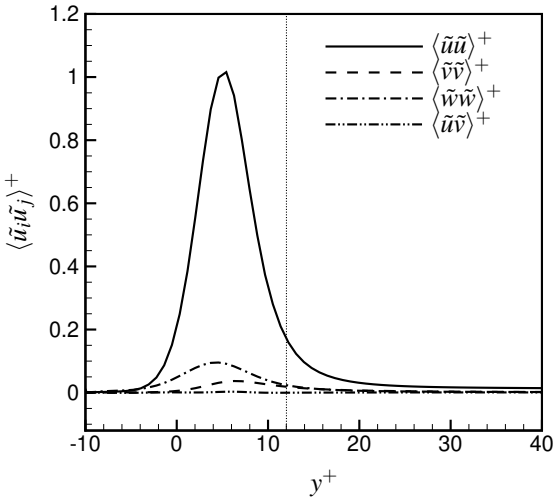

Figure 8: Normal and shear components of dispersive stress tensor.

The spatially-averaged Reynolds stresses and dispersive stresses are shown in figure 7, scaled by $(u_\tau^b)^2$. The profiles of Reynolds stresses are compared to the smooth case in the near-wall region. The peak of $\langle\overline{u'u'}\rangle^+$ is decreased in the rough case while the outer part collapses well with the smooth case. The other components $\langle\overline{v'v'}\rangle^+$, $\langle\overline{w'w'}\rangle^+$ and $\langle\overline{u'v'}\rangle^+$ do not show as much difference as $\langle\overline{u'u'}\rangle^+$ since the flow is at the onset of the transitionally rough regime. Obviously, the magnitude of dispersive stresses is much smaller than the Reynolds stresses, and are negligible above the rough region.

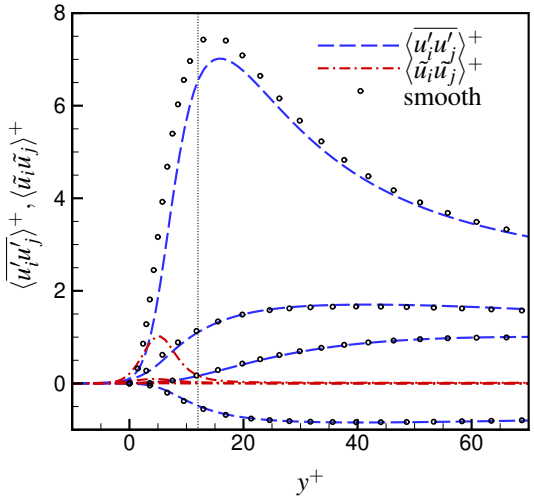

Figure 7: Reynolds and dispersive stresses in the near-wall region.

Figure 8 shows a closer view of the components of dispersive stress tensor. The levels of dispersive stress are less than those of the irregular roughness investigated by Jelly and Busse (2019), which is related to the smaller roughness Reynolds number of Case $k_{rms} \approx 88\mu m$. The profile of $\langle\tilde{u}\tilde{u}\rangle^+$ reaches maximum at $y^+ = 6$ and drops to zero at $y^+ = 30$, underlining the spatial inhomogeneity near the rough-wall region. The profiles of $\langle\tilde{v}\tilde{v}\rangle^+$, $\langle\tilde{w}\tilde{w}\rangle^+$ and $\langle\tilde{u}\tilde{v}\rangle^+$ have the similar trend as $\langle\tilde{u}\tilde{u}\rangle^+$, but smaller magnitudes.

Rough wall-pressure fluctuations

Next, we investigate the mean-square pressure fluctuations $\langle\overline{p'p'}\rangle^+$ of Case $k_{rms} \approx 88\mu m$. In figure 9, the profile of $\langle\overline{p'p'}\rangle^+$ of Case $k_{rms} \approx 88\mu m$ as well as that in the smooth channel flow at three different Re_τ are shown. As Re_τ increases, the level of pressure fluctuations is increased before decreasing into the logarithmic matching law fitted by Panton et al. (2017).

$$\langle\overline{p'p'}\rangle^+_{cp}(y/\delta) = -2.5625\ln(y/\delta) + 0.2703 \qquad (8)$$

For Case $k_{rms} \approx 88\mu m$, $\langle\overline{p'p'}\rangle^+$ shows a higher level in the roughness sublayer compared to Case Smooth at the same Re_τ before collapsing onto the logarithmic profile. To further examine the large values of pressure fluctuations in the rough region, the distribution of $\langle\overline{p'p'}\rangle^+$ is examined at $y^+ = 3$ in figure 10. The high pressure fluctuations occurs in front of the roughness asperities, while the wake regions behind the rough elements show a lower level of pressure fluctuations.

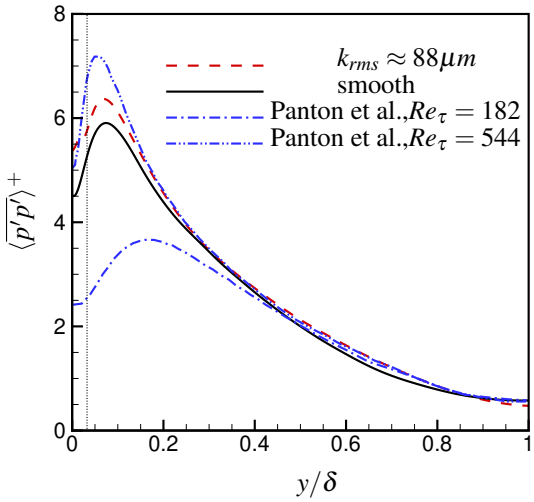

Figure 9: Mean-square pressure fluctuations against wall-normal distance in the outer coordinate.

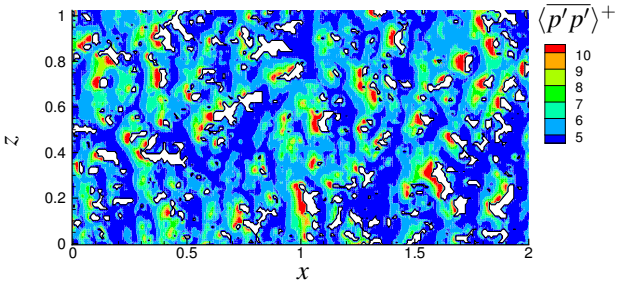

Figure 10: Pressure fluctuation $\langle \overline{p'p'} \rangle^+$ at $y^+ = 3$.

To better understand the pressure fluctuation in the rough case, the contribution of the source terms in the Poisson's equation is investigated. The Poisson's equation for the fluctuating pressure obtained by subtracting the mean from the instantaneous pressure is,

$$\frac{\partial^2 p'}{\partial x_i \partial x_i} = -2\frac{\partial \langle \overline{u_i} \rangle}{\partial x_j}\frac{\partial u_j'}{\partial x_i} - \frac{\partial^2}{\partial x_i \partial x_j}(u_i'u_j' - \overline{u_i'u_j'}). \quad (9)$$

The first term on the right-hand side is called the mean-shear source term (MS) and the second term is known as the turbulence-turbulence source term (TT). In the smooth-wall channel flow, the contribution of the mean-shear source term is the component, $MS_{12} = -2\frac{\partial \langle \overline{u} \rangle}{\partial y}\frac{\partial v'}{\partial x}$. Since this term is weighted by the temporal and spatial-averaged streamwise velocity gradient, it can present different distribution in the rough case. Chang III et al. (1999) suggested that the dominant turbulence-turbulence source term TT_{23} is related to horseshoe vortices.

The mean velocity gradient, root-mean-square (rms) MS_{12} and TT_{23} are examined in figure 11. For Case Smooth, the mean velocity gradient shows maximum at the wall, while MS_{12} presents its maximum at $y^+ = 11$. For Case $k_{rms} \approx 88\mu m$, the rms of MS_{12} is enhanced in the roughness layer, reaches the peak value at $y^+ = 5$, decreases and collapses onto the profile of the smooth case. It is also found that the maximum of rms MS_{12} for Case $k_{rms} \approx 88\mu m$ is at the same peak location as the mean velocity gradient. Compared to MS_{12}, the increased level of TT_{23} is smaller and mainly occurs in the roughness layer.

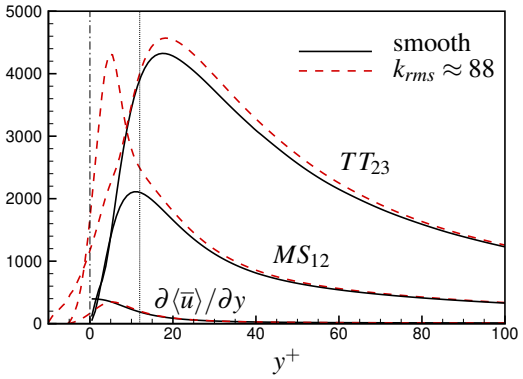

Figure 11: Profiles of the mean velocity gradient, dominant mean-shear and turbulence-turbulence source terms against the wall-normal distance.

The local variations of rms MS_{12} and TT_{23} in the near-wall region are examined in figure 12(a) and (b). The intense and high-magnitude MS_{12} occurs in front of the roughness protrusions and on the crests. The high-magnitude TT_{23} are identified in two regions, labeled by A and B. At location A, TT_{23} is large in the immediate vicinity upstream of the roughness protrusion. Figure 12(c) and (d) show the time-averaged streamwise vorticity at the same regions. A pair of streamwise vortices is observed at the same location which is induced by the upward velocity in front of the protrusions. A pair of secondary vortices is observed below the induced streamwise vortices, closely attaching to the bottom wall. At location B, the high-magnitude streak is found to be located in the valley where the streamwise vortices occur. These observations show the high correlation between TT_{23} and the quasi-streamwise vortices. It can be concluded that the shear layer along with the "roll-up" motion generated at the upstream stagnation point of the protrusion is a primary source of the larger pressure fluctuations, while the streamwise vortices that occur in front of the protrusion and in the troughs, generating secondary vortical structures below the main vortices, also

make a contribution to the increased pressure fluctuations in the rough-wall flows.

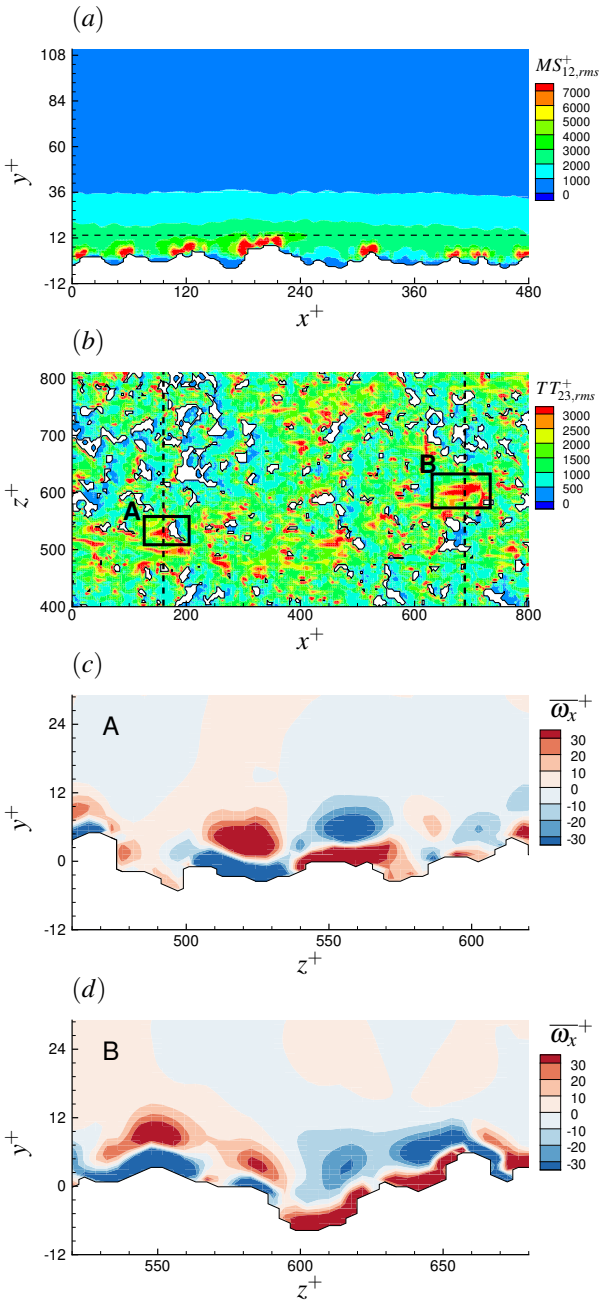

Figure 12: (a) Spatial variation of rms MS_{12} at $z^+ = 628$, (b) Spatial variation of rms TT_{23} at $y^+ = 3$. Time-averaged streamwise vorticity $\overline{\omega_x}$ normalised by u_τ/δ corresponding to (c) region A at $x^+ = 160$, (d) region B at $x^+ = 688$. The dashed lines in (b) denote the z^+-y^+ planes observed in (c) and (d). Note for the z^+-y^+ plane, the mean flow direction points out of the page.

Sources of smooth wall-pressure fluctuations

For the smooth-wall case, the wall pressure fluctuations is from the spatially homogeneous fluid sources alone. We investigate this further using a novel framework (Anantharamu and Mahesh, 2020) that combines the Green's function solution to the pressure fluctuation Poisson equation, DNS data and spectral POD (Proper Orthogonal Decomposition).

The DNS data set used for the smooth wall-pressure source investigation is from a separate set of turbulent channel flow simulations at $Re_\tau = 180$ and 400. These simulations used a moving frame of reference to reduce the dispersive errors, and a larger computational box to include the contribution of large scale structures to wall-pressure PSD (power spectral density). For further details of these simulations, we refer the reader to Anantharamu and Mahesh (2020).

The goal is to express the wall-pressure PSD as a double wall-normal integral of a cross-spectral density (CSD). The pressure fluctuation at a point $(x,-\delta,z)$ on the wall can be expressed as a wall-normal integral using the Green's function as

$$p(x,-\delta,z,t) = \int_{-\delta}^{+\delta} f_G(x,y,z,t)\,\mathrm{d}y,$$
$$f_G(x,y,z,t) = \iint_{-\infty}^{+\infty} G(-\delta,y,k_1,k_3)\hat{f}(k_1,y,k_3,t)e^{i(k_1x+k_3z)}\,\mathrm{d}k_1\mathrm{d}k_3, \tag{10}$$

where $f_G(x,y,z,t)$ is called the 'net source' function, $G(-\delta,y,k_1,k_3)$ and $\hat{f}(k_1,y,k_3,t)$ is the Green's function at the bottom wall and the spatial Fourier transform of the right hand side of the pressure fluctuation Poisson equation, respectively. We can show that the wall-pressure PSD $\phi_{pp}(\omega)$ relates to the net source $f_G(x,y,z,t)$ as

$$\phi_{pp}(\omega) = \iint_{-\delta}^{+\delta} \Gamma(r,s,\omega)\,\mathrm{d}r\,\mathrm{d}s,$$
$$\Gamma(r,s,\omega) = \frac{1}{2\pi}\int_{-\infty}^{\infty} \langle f_G^*(x,r,z,t) f_G(x,s,z,t+\tau)\rangle e^{-i\omega\tau}\mathrm{d}\tau, \tag{11}$$

where $\Gamma(r,s,\omega)$ is the CSD of the net source $f_G(x,y,z,t)$. $\Gamma(r,s,\omega)$ gives the contribution of each wall-parallel plane pair (r,s) to the wall-pressure PSD as a function of frequency. We can also show that $\Gamma(r,s,\omega)$ relates to the four-dimensional CSD of the pressure Poisson fluctuation source term $f(x,y,z,t)$ as

$$\Gamma(r,s,\omega) = \iint_{-\infty}^{+\infty} G^*(0,r,\mathrm{k}_1,\mathrm{k}_3)G(0,s,\mathrm{k}_1,\mathrm{k}_3)\,\varphi_{ff}(r,s,k_1,k_3,\omega)\mathrm{d}\mathrm{k}_1\,\mathrm{d}\mathrm{k}_3. \tag{12}$$

To obtain the contribution from a plane $y = r$ to the wall-pressure PSD, we integrate Γ along s and obtain,

$$\phi_{pp}(\omega) = \int_{-\delta}^{+\delta} \Psi(r,\omega)\,\mathrm{d}r, \tag{13}$$

where

$$\Psi(r,\omega) = \int_{-\delta}^{+\delta} \Gamma(r,s,\omega)\mathrm{d}r \tag{14}$$

It can be shown that $\Psi(r,\omega)$ is the CSD of the net source $f_G(x,y,z,t)$ and the wall-pressure fluctuation $p(x,-\delta,z,t)$, i.e.,

$$\Psi(r,\omega) = \frac{1}{2\pi}\int_{-\infty}^{\infty} \langle f_G^*(x,r,z,t)p(x,-\delta,z,t+\tau)\rangle e^{-i\omega\tau}\mathrm{d}\tau. \tag{15}$$

Hence, we call $\Psi(r,\omega)$ as the wall-pressure - net source CSD. We compute the net CSD $\Gamma(r,s,\omega)$ (equation 12) using the three-dimensional DNS data at $Re_\tau = 180$ and 400. For a streaming parallel implementation procedure to compute $\Gamma(r,s,\omega)$, we refer the reader to Anantharamu and Mahesh (2020). Further, we compute the wall-pressure net source CSD $\Psi(r,\omega)$ from the computed net source CSD $\Gamma(r,s,\omega)$ using equation 14.

We will first discuss the inner peak of the premultiplied wall-pressure PSD. Then, we identify the location and features of the dominant source that contributes to this inner peak using the computed $\Psi(r,\omega)$ (see equation 11).

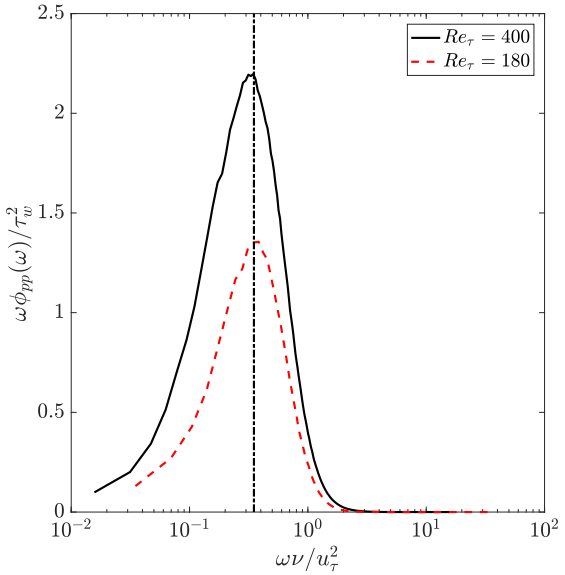

Figure 13: Premultiplied wall-pressure PSD for $Re_\tau = 180$ and 400.

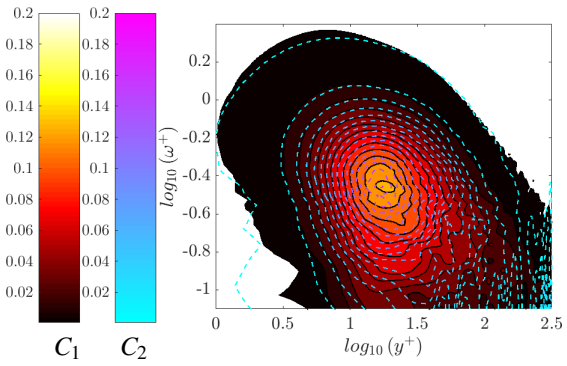

Figure 14: Real part of premultiplied wall-pressure-NS CSD $(y^+\omega^+ Re(\Psi(y^+,\omega^+))/\langle p^2\rangle)$ for $Re_\tau = 400$ (black solid lines with filled contours with colormap C_1) and 180 (line contours with colormap C_2). Contour lines are 20 equally spaced values between 4e-4 and 2e-1.

Figure 13 shows the premultiplied wall-pressure PSD for $Re_\tau = 180$ and 400. At these low Reynolds numbers, we clearly see the inner peak at $\omega^+ \approx 0.35$ whose frequency scales in inner units. This peak has been observed before by Hu et al. (2006) and Panton et al. (2017) up to Reynolds numbers of $Re_\tau \approx 5000$.

To identify the location of the dominant sources that contribute to this inner peak, we plot the contours of the real part of wall-pressure - net source CSD ($\Psi(r,\omega)$) in premultiplied form in figure 14. The filled contours with colormap C_1 is for $Re_\tau = 400$ and the line contours with colormap C_2 is for $Re_\tau = 180$. The coordinates of the peak value in the contours are (y_p^+, ω_p^+) of $(16.5, 0.35)$ for $Re_\tau = 180$ and $(18.4, 0.35)$ for $Re_\tau = 400$. The frequency coordinate of the peak contour value coincides with the pre-multiplied PSD peak shown in figure 13. The corresponding wall-normal peak coordinates lie in the buffer layer and is approximately the same in inner units. This quantitatively shows that the location of the sources that contribute to the premultiplied PSD peak at $\omega^+ \approx 0.35$ is in the buffer layer. Further, one cannot expect the wall-normal coordinates to completely scale in inner units because the CSD $\Psi(r,\omega)$ has integrated contribution from the sources in the outer region of the channel also (see equation 14).

We obtain the phase difference between the wall-pressure fluctuation and the dominant source using the argument of $\Psi(y_p^+,\omega^+)$. The phase difference is 0.013π for $Re_\tau = 180$ and 0.016π for $Re_\tau = 400$. The values are very small indicating that the wall-pressure is almost in-phase with these dominant sources.

We would like to mention that this location of the dominant source at $\omega^+ \approx 0.35$ could not be identified using the net source PSD $\Gamma(r,r,\omega)$. The contours of $\Gamma(r,r,\omega)$ did not show a distinct peak at $\omega^+ = 0.35$ that

approximately coincided in y^+ for the two Re_τ. This points to the fact that the interference of the contribution from different wall-normal regions plays a major role in determining the peak wall-normal location.

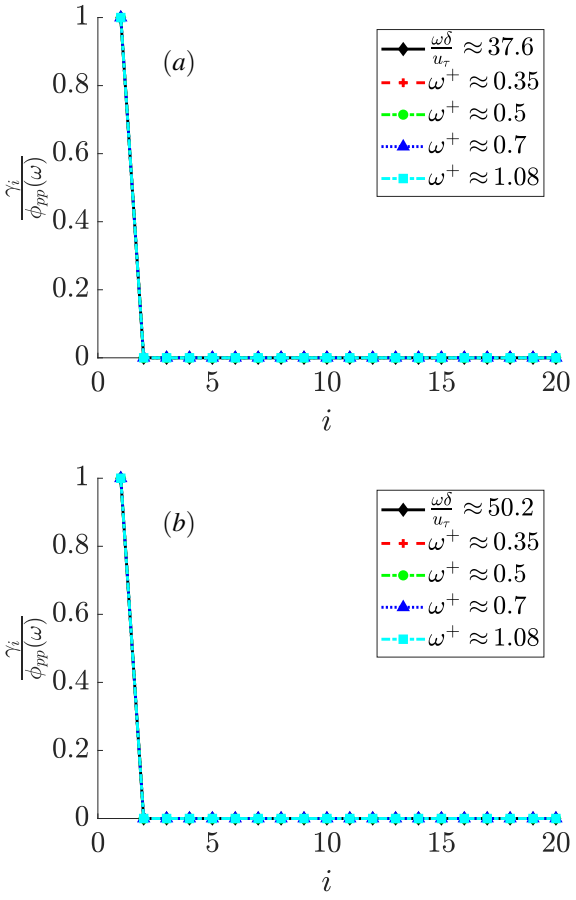

Figure 15: Fractional contribution of each spectral POD mode ($\gamma_i(\omega)$) to the wall-pressure PSD for (a) $Re_\tau = 180$ and (b) $Re_\tau = 400$.

Next, we identify the decorrelated features of the sources using spectral Proper Orthogonal Decomposition. We will use the obtained spectral POD modes to further examine the features of the dominant source. Using spectral POD, we can decompose the net source CSD $\Gamma(r,s,\omega)$ as

$$\Gamma(r,s,\omega) = \sum_{i=1}^{\infty} \lambda_i(\omega)\Phi_i(r,\omega)\Phi_i^*(s,\omega). \tag{16}$$

Here, $\{\lambda_i(\omega)\}_{i=1}^{\infty}$ are the spectral POD eigenvalues and $\{\Phi_i(y,\omega)\}_{i=1}^{\infty}$ are the spectral POD modes. To identify the sources that are pertinent to the wall-pressure PSD, we require the modes to be orthogonal in an inner product with a symmetric positive definite kernel instead of the commonly used L^2 inner product. For details on the spectral POD computation, we refer the reader to Anantharamu and Mahesh (2020).

The contribution of each spectral POD mode to wall-pressure PSD is $\gamma_i(\omega)$, i.e.,

$$\phi_{pp}(\omega) = \sum_{i=1}^{\infty} \gamma_i(\omega). \tag{17}$$

We can show that

$$\gamma_i(\omega) = \lambda_i(\omega)\left|\int_{-1}^{+1} \Phi_i(r,\omega)\,\mathrm{d}r\right|^2; i = 1,\ldots,\infty, \tag{18}$$

which can be simplified to yield

$$\gamma_i(\omega) = \lambda_i(\omega) \left(\int_{-1}^{+1} |\Phi_i(r,\omega)| cos\left(\angle\Phi_i(r,\omega) - \angle\Phi_i^n(\omega)\right)\mathrm{d}r\right)^2 ; i = 1,\ldots,\infty, \tag{19}$$

where $\angle\Phi_i^n(\omega) = \angle\left(\int_{-\delta}^{+\delta}\Phi_i(y,\omega)\,\mathrm{d}y\right)$. From the above equation, we observe that the eigenvalue, magnitude and phase of the spectral POD mode, all play a role in determining its contribution to the wall-pressure PSD. Fluid sources contained in wall-normal regions with phase in the range $|\angle\Phi_i(y,\omega) - \angle\Phi_i^n(\omega)| < \pi/2$ undergo destructive interference with the sources in the region where $\pi/2 < |\angle\Phi_i(y,\omega) - \angle\Phi_i^n(\omega)| < \pi$. This interference of the fluid sources from different wall-normal region plays an important role in determining the net contribution of a spectral POD mode to the wall-pressure PSD.

Figure 15 shows the fractional contribution ($\gamma_i(\omega)$) of each spectral POD mode to the wall-pressure PSD for different frequencies. Figure 15a is for $Re_\tau = 180$ and figure 15b is for $Re_\tau = 400$. Clearly, we observe that the identified dominant mode contributes to nearly all the wall-pressure PSD. For the remaining modes, the contribution from different wall-normal regions undergo destructive interference yielding net zero contribution. Therefore, the dominant mode is the active source that constitutes the entire wall-pressure PSD. The remaining modes are inactive, in the sense that they do not contribute to the wall-pressure PSD due to the destructive interference. Further, the active and inactive parts are decorrelated because they stem from different spectral POD modes. Next, we analyze the active contribution further by examining the envelope and phase of the dominant spectral POD mode.

Figure 16 shows the envelope of the dominant spectral POD mode for the two Re_τ. We show the envelopes for the premultiplied peak frequency $\omega^+ \approx 0.35$ and a few other high frequencies ($\omega^+ \approx 0.5, 0.7,$ and 1.08). The wall-normal distances in the two figures are in inner units. The envelope's shape indicates that

the sources are primarily confined near to the wall. The intensities peak in the buffer region of the channel similar to the wall-pressure - net source CSD $\Psi(y,\omega)$. With increasing frequency, the peak moves closer to the wall and the envelope's width decreases. This further restricts the sources to a smaller near-wall region. Further, the peak locations and the envelope shapes are very similar for the two Reynolds numbers. This supports the case that at the premultiplied peak and higher frequencies, the wall-pressure sources appear to scale better in inner units.

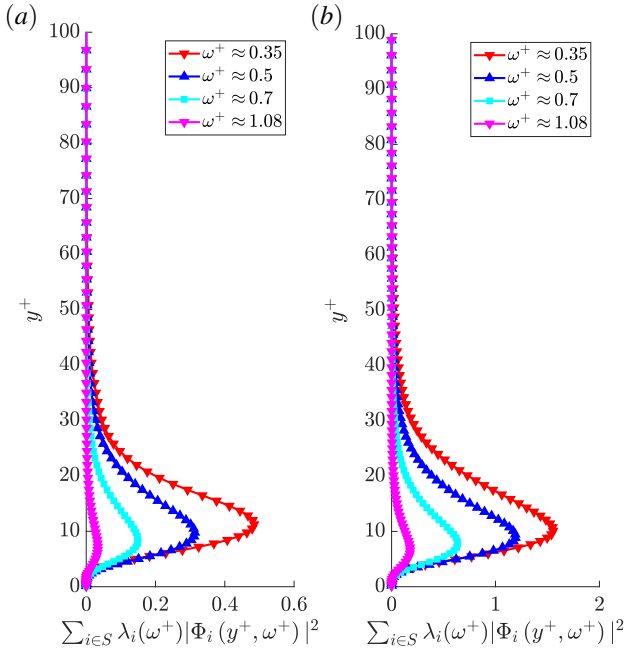

Figure 16: Envelope (magnitude) of the dominant spectral POD mode for (a) $Re_\tau = 180$ and (b) $Re_\tau = 400$ for different frequencies.

Figure 17 shows the phase of the dominant spectral POD mode for the same frequencies plotted in 16. The phase primarily lies in the range $|\angle\Phi_i - \angle\Phi_i^n| < \pi/2$ (between the two vertical black dashed lines). Therefore, the contributions from different wall-normal regions mainly undergo constructive interference (see equation 19). This reinforcing mechanism is what plays a significant role in making the dominant spectral POD mode the major contributor to the wall-pressure PSD.

The slope of the wall-normal phase variation in figure 17 is mainly negative. The negative slope is indicative of a convecting coherent structure inclined in the downstream direction. To establish this connection, we construct a representative net source field $\tilde{f_G}(x,y,z,t)$ at the premultiplied peak frequency $\omega_o^+ \approx 0.35$. We do so by using the dominant spectral POD mode $\Phi_1(y,\omega)$ as

$$\tilde{f_G}(x,y,z,t) = Re(\alpha(x,z,\omega_o)e^{-i\angle\Phi_1(y,\omega_o)}|\Phi_1(y,\omega_o)|e^{i\omega_o t}), \tag{20}$$

where $\alpha(x,z,\omega_o)$ is the coefficient. Intuitively, one can expect the $e^{-i\omega_o x/c_o(\omega_o)}$ Fourier component of $\alpha(x,z,\omega_o)$ to be the dominant one, where $c_o(\omega_o)$ is the streamwise convective velocity. Therefore, we set $\alpha(x,z,\omega_o) = e^{-i\omega_o x/c_o(\omega_o)}$. We use a convective velocity of $c(\omega_o) = \omega_o/k_p(\omega_o)$, where $k_p(\omega_o)$ is the peak wavenumber of the wall-pressure streamwise wavenumber frequency spectrum at frequency ω_o. We set time t to zero. Figure 18 shows the constructed net source field for the two Re_τ. The representative field resembles a coherent structure inclined in the downstream direction.

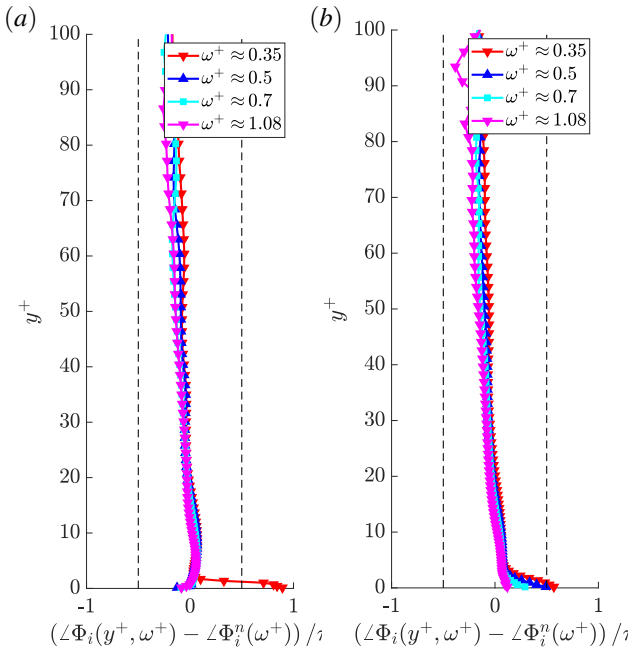

Figure 17: Phase of the dominant spectral POD mode for (a) $Re_\tau = 180$ and (b) $Re_\tau = 400$ for different frequencies.

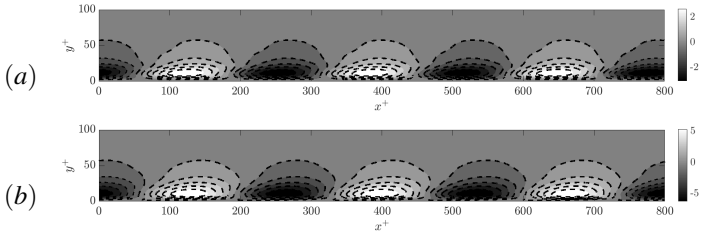

Figure 18: Representative net source field ($\tilde{f_G}(x,y,z,t)$) ($\gamma_i(\omega)$) constructed using the dominant spectral POD mode at the premultiplied peak frequency $\omega^+ \approx 0.35$ for (a) $Re_\tau = 180$ and (b) $Re_\tau = 400$.

Overall, the framework presented here quantitatively identifies the contribution of different wall-normal locations to the wall-pressure PSD as a function of frequency. This is the first analysis that accounts for the interference of the sources from different wall-normal regions. The analysis supports the case that the wall-pressure sources can be decomposed into two decorrelated components - active and inactive. The active portion composed of the dominant spectral POD mode contributes to the entire PSD. The inactive portion composed of the sub-optimal spectral POD modes does not contribute to the PSD. This is due to destructive interference of the contributions from different wall-normal regions for the sub-optimal modes. A representative reconstruction of the wall-pressure source at the premultiplied peak frequency using the dominant spectral POD mode resembles a downstream inclined coherent structure. Currently, we are working on extending the above analysis framework to rough walls.

Gibbs energy minimization results

In this section, the prediction of equilibrium interfacial shapes over rough surfaces will be discussed. Specifically, the robustness of the algorithm is demonstrated for a variety of geometries such as a 3D wavy substrate, longitudinal grooves, posts, randomly generated roughness and a real surface scan.

3D **Longitudinal Grooves**

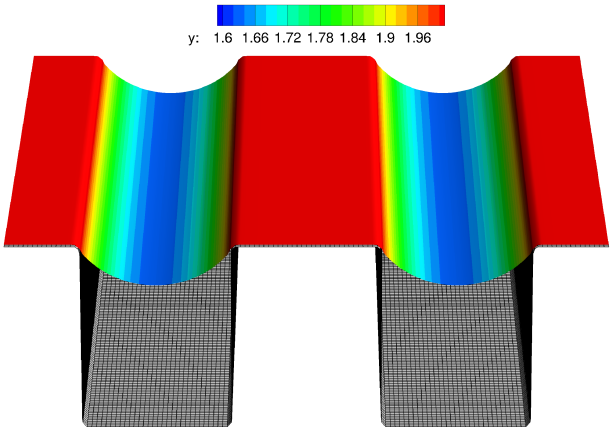

Figure 19: Equilibrium interface location for a 3D grooved substrate where the gray isosurface represents the rigid substrate, and the zero level set that represents the interface is colored by the height isocontours.

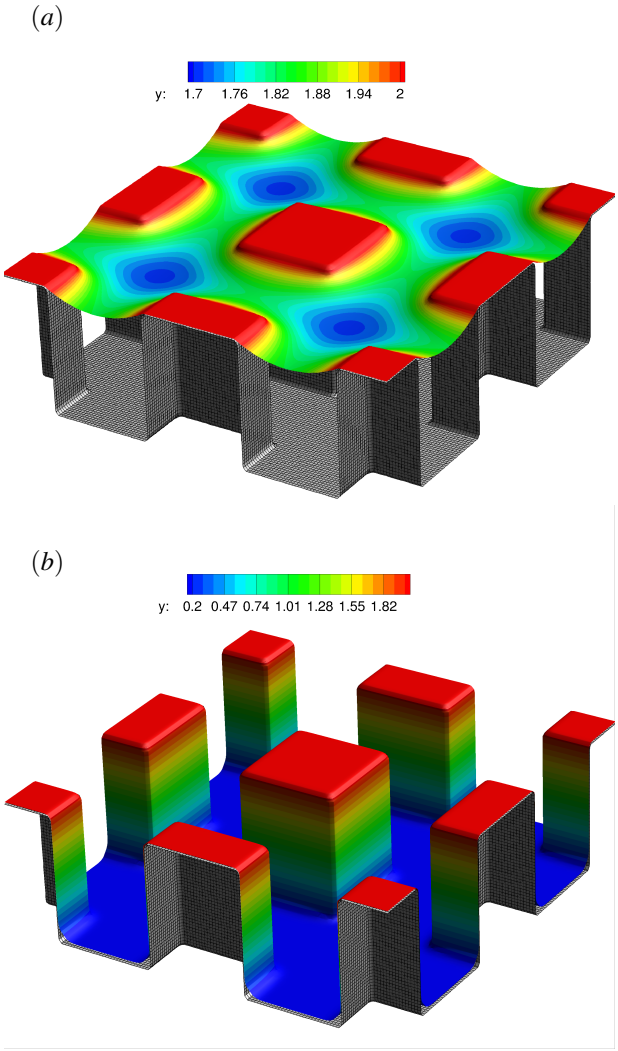

Figure 20: Equilibrium interface location for post geometries, the gray isosurface represents the rigid substrate, the zero level set that represents the interface is colored by the height isocontours. (a) Equilibrium shape for $\Delta p = 0.5$ and (b) interfacial failure at $\Delta p = 1$ where the liquid completely wets the cavities of the post.

Consider a rough substrate representing a 3D longitudinal groove. The level set that represents the solid is given by:

$$\psi(\mathbf{x}) = (y-1) - \text{sign}\big[1, \cos(2x)\big]\,. \tag{21}$$

The domain extents are $[L_x, L_y, L_z] = [2\pi, 3, 2\pi]$ and the grid size is $N_x \times N_y \times N_z = 128 \times 62 \times 128$ for the 3D case. The time-step is taken to be $dt = 10^{-5}$ and $\alpha = 0.4$. The external pressure is $\Delta p = 1$, and the non-dimensional interfacial surface tension is $\tau_{LA} = 1$. Young-Laplace gives a radius of curvature $R_{analytic} = 1$. Figure 19 shows the computed interface. The error in the radius of curvature computed numerically is 0.7% when compared

to the analytic solution of Young-Laplace.

Grooved Posts

We make use of the Boolean operations in order to represent the post geometry. Consider the level sets that represent the solid:

$$\psi_1(\mathbf{x}) = (y-1) - \text{sign}\big[1, \cos(2x)\big]\,. \tag{22}$$

The above equation represents longitudinal grooves in the $x-y$ plane extending in the $z-$direction, and similarly in the $y-z$ plane extending in the $x-$direction, the level set is given by:

$$\psi_2(\mathbf{x}) = (y-1) - \text{sign}\big[1, \cos(2z)\big]\,. \tag{23}$$

The intersection $\psi = \psi_1 \cap \psi_2$ defined such that

$$\psi(\mathbf{x}) = \max(\psi_1, \psi_2) \tag{24}$$

gives the level set for posts. The domain extents are $[L_x, L_y, L_z] = [2\pi, 3, 2\pi]$ and the grid size is $N_x \times N_y \times N_z = 128 \times 62 \times 128$. The time-step is $dt = 10^{-5}$ and $\alpha = 0.4$. The simulation is done at two different external pressure values, $\Delta p = 0.5$ and $\Delta p = 1$. The aim is to demonstrate the prediction of interfacial failure. At $\Delta p = 0.5$ equilibrium is observed. However, when the value for pressure is doubled, the interface is no longer pinned, the interface fails and fills up the grooves. This process is known as depinned recession.

3*D* Wavy Substrate

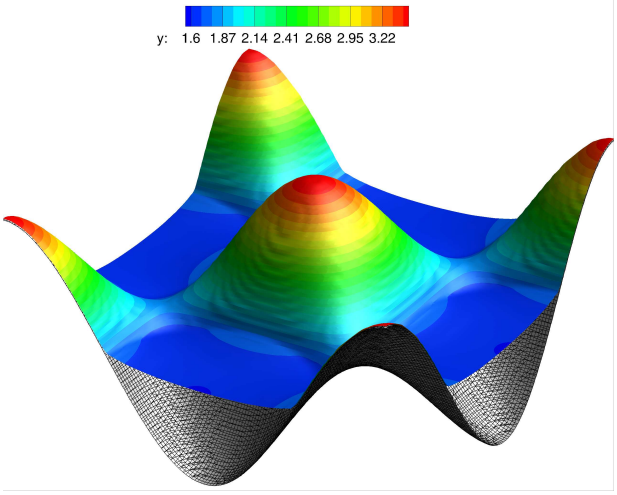

Figure 21: Equilibrium interface location for a 3D cosine substrate. The gray isosurface represents the rigid substrate, and the zero level set that represents the interface is colored by the height isocontours.

Consider a three-dimensional wavy substrate that is given by the following level set:

$$\psi(\mathbf{x}) = (y - 2h_{cr}) - 2h_{cr}\cos(x)\cos(z)\,, \tag{25}$$

where $h_{cr} = -\tan\theta_Y$ and $\theta_Y = 140^\circ$ (Youngs contact angle). The domain extents are $[L_x, L_y, L_z] = [2\pi, 3, 2\pi]$ and the grid size is $N_x \times N_y \times N_z = 128 \times 62 \times 128$. The time-step is $dt = 10^{-5}$ and $\alpha = 0.4$. The interface level set is initialized at a height of $y = 2.5$. The external pressure prescribed is $\Delta p = 0.2$. The interface evolves and moves down towards the solid substrate, the Gibbs energy is monitored until it reaches steady state indicating that the solution is in equilibrium.

Random Roughness

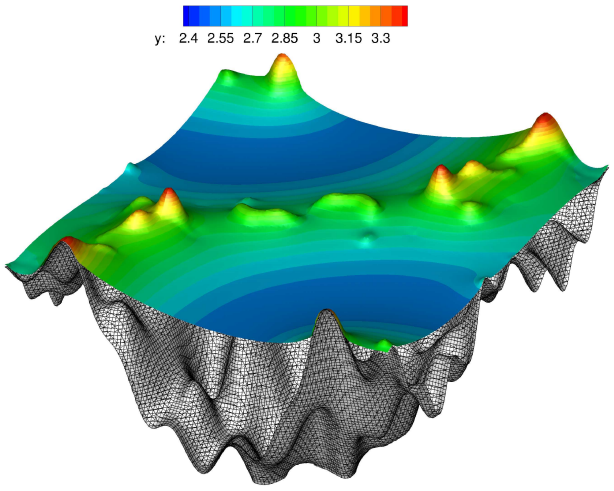

Figure 22: Equilibrium interface location for a random rough substrate for a loading condition of $\Delta p = 0.2$. The gray isosurface represents the rigid substrate. The zero level set represents the interface and is colored by the height isocontour.

The random rough surface is generated using a fractal dimension β. A composition of many elementary waves in the form of $\cos(\mathbf{k}\cdot\mathbf{x} + \varphi)$ is specified. A range of amplitudes that tapers off based on a certain distribution is given by:

$$h_{mn} = \frac{1}{(m^2+n^2)^{\beta/2}}\,, \tag{26}$$

where m and n are the wavenumbers. A Gaussian distribution g_{mn} is used to get a smooth random variation in amplitude where the amplitude distribution is given by:

$$A_{mn} = g_{mn} h_{mn}\,. \tag{27}$$

The phase angle is also sampled from a Gaussian distribution and is scaled such that it varies between $-\pi/2$ and $\pi/2$:

$$\varphi_{mn} = \frac{\pi}{2} g_{mn}\,. \tag{28}$$

By taking a double sum over the wavenumbers in both spatial directions, the rough surface height distribution is then given by:

$$h_f(\mathbf{x}) = \sum_{m,n} A_{mn} \cos(k_{mn} \cdot \mathbf{x} + \varphi_{mn}) . \tag{29}$$

The height distribution is scaled such that the maximum height from peak to valley is $2h_{cr}$. Then the level set that represents the solid is given by:

$$\psi(\mathbf{x}) = (y - 2h_{cr}) - h_f(\mathbf{x}) \tag{30}$$

For this simulation, $N = 10$ is taken for the spatial frequency resolution, and $\beta = 1.5$ is chosen to represent a peak dominant surface. The domain extents are $[L_x, L_y, L_z] = [2\pi, 3, 2\pi]$ and the grid size is $N_x \times N_y \times N_z = 128 \times 62 \times 128$. The time-step is $dt = 10^{-5}$ and $\alpha = 0.4$. The external pressure is $\Delta p = 0.2$. This example demonstrates the ability of the algorithm to handle rough surfaces in a robust manner.

Real scanned roughness

The original surface scan was scaled in this corresponding case such that the maximum peak to valley is unity. The domain extents are $[L_x, L_y, L_z] = [2\pi, 1.3, 2\pi]$ and the grid size is $N_x \times N_y \times N_z = 256 \times 52 \times 256$. The time-step is $dt = 10^{-5}$ and $\alpha = 0.4$. The external pressure is $\Delta p = 0.1$ and $\theta_Y = 140^\circ$. Figure 23 shows the obtained equilibrium interface over the surface scan.

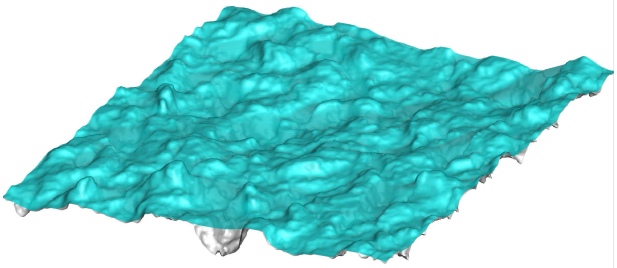

Figure 23: Equilibrium interface location for a real surface scan. The gray isosurface represents the rigid substrate, the zero level set shown in the cyan color represents the interface.

The algorithm is able to handle complicated geometries obtained from real surface scans in a robust manner. This allows for a large parametric studies to be explored for different rough surfaces under different loading conditions. It also opens up the ability to compare to experiments. The evolution of the interface as it goes to equilibrium is shown in figure 24, the interface is colored by the height isocontour as it evolves in time to reach its equilibrium position.

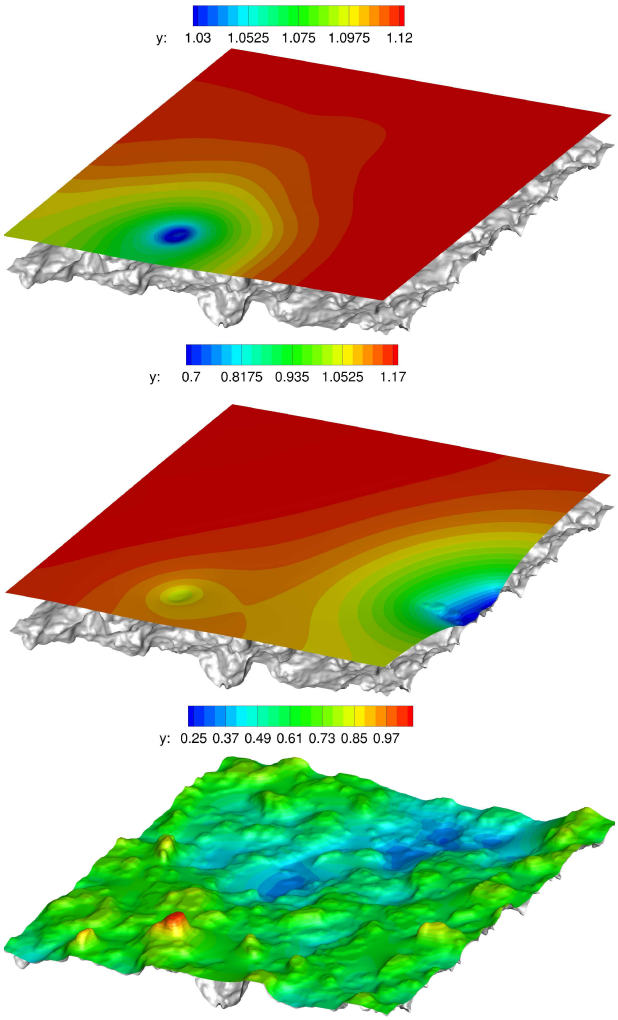

Figure 24: Equilibrium interface location for a real surface roughness obtained from a scan for a loading condition of $\Delta p = 0.1$. The gray isosurface represents the rigid substrate. The zero level set represents the interface and is colored by the height isocontour. The images are a sequential motion as the interface evolves from the initial condition to equilibrium.

SUMMARY

DNS of turbulent channel flow at $Re_\tau = 400$ is performed, where the bottom wall is a realistically rough surface. Simulations of turbulent smooth channel flow are also performed as a baseline. Good agreement is obtained for the skin friction coefficient between our simulation and the experiments.

To investigate the spatial variation of the time-average flow field, the double-averaging decomposition is used. The mean velocity profile $\langle \overline{u} \rangle$ shows a slip velocity at the wall and an offset from the smooth-wall profile for the whole region. The

form-induced velocity field in the rough layer shows that large positive $\tilde{u}$ occurs in the comparatively larger trough regions while large negative $\tilde{u}$ occurs in the wake regions behind the roughness elements. Large positive $\tilde{v}$ is observed in front of the roughness asperities, corresponding to the impulsive upward velocity of the fluid due to the roughness peaks. The pairs of streamwise vortices produced by this upward velocity can also be found in front of the roughness elements in the contour of $\tilde{w}$. The pressure field indicates that the form drag is mainly generated by the roughness peaks.

The Reynolds and dispersive stresses are examined for the realistic surface. The most significant difference is that the peak of $\langle\overline{u'u'}\rangle$ is smaller compared to the smooth case when normalized by the local friction velocity $(u_\tau^b)^2$. The magnitude of dispersive stresses is much smaller than that of Reynolds stresses and is almost negligible above the rough layer. The mean-square pressure fluctuations are enhanced in the near-wall region. The higher pressure fluctuations are observed in front of the roughness asperities, indicating that the roughness protrusions are an important source of the increased pressure fluctuations. The dominant mean-shear and turbulence-turbulence source terms of the Poisson's equation are examined. The results suggest that the shear layer induced by roughness protrusions, the streamwise vortices and secondary flow interactions among the roughness elements make a contribution to the increased pressure fluctuations in the rough-wall flows.

We analyse the smooth wall-pressure fluctuation sources using a novel framework. The analysis reveals the importance of buffer layer sources for both $Re_\tau = 180$ and 400 wall-pressure fluctuations. This result has implications in the context of wall-modeled large eddy simulations (LES) where the buffer layer is not resolved. Thus, additional modeling specific to wall-pressure fluctuation is essential in wall-modeled LES. Spectral POD of the source terms reveals the importance of constructive/destructive interference of wall-normal sources to wall-pressure PSD. The decomposition separates the sources into two categories - active and inactive. The active component comprised by the dominant contributes to the entire wall-pressure PSD. The inactive components comprised by the remaining sub-optimal modes do not contribute to the wall-pressure PSD. Their contribution from different wall-normal regions undergo destructive interference resulting in zero net contribution. Further, representative net source field constructed using the dominant spectral POD mode resembles a coherent structure inclined in the downstream direction.

In the context of energy minimization, the original algorithm is shown to handle a wide range of geometries that include structured surfaces, wavy substrates, and random roughness. We extend the original analysis to handle realistic roughness obtained from surface scans. This adds a great deal of flexibility to investigate a wide range of parameter space for predicting the equilibrium positions of liquid-air interfaces. It also allows for the comparison to experimental surface scan measurements. The height isocontours can be overlayed on the interface to show a height map of its equilibrium location. This metric can be used as an indicator to the largest Gibbs energy location, this would help predict where the interface is most susceptible to failure. Another application is coupling the gas fraction associated with each equilibrium solution from different external pressures to existing slip models.

ACKNOWLEDGEMENTS

This work was supported by the United States Office of Naval Research (ONR) Grant N00014-17-1-2308 managed by Drs. J. Gorski, T. Fu and P. Chang, N00014-17-1-2939 and N00014-17-1-2676 with Dr. Ki Han Kim as technical monitor. Computing resources were provided by the Minnesota Supercomputing Institute (MSI), and US Army Engineer Research and Development Center (ERDC) in Vicksburg, Mississipi on the Cray X6, Copper and Onyx of the High Performance Computing Modernization Program. We are grateful to Professor K. Flack at the United States Naval Academy for providing us with the scanned surface data used in the present work, to Professor W. Choi at the University of Texas Dallas and Professor G. H. McKinley at MIT for providing the scanned surface data used in the Gibbs energy minimization.

REFERENCES

Alamé, K., Anantharamu, S., and Mahesh, K. "A variational level set methodology without reinitialization for the prediction of equilibrium interfaces over arbitrary solid surfaces". Journal of Computational Physics, page 109184, 2019.

Anantharamu, S. and Mahesh, K. "Analysis of wall-pressure fluctuation sources from direct numerical simulation of turbulent channel flow". Journal of Fluid Mechanics, 898:A17, 2020.

Bottiglione, F. and Carbone, G. "Role of statistical properties of randomly rough surfaces in controlling superhydrophobicity". Langmuir, 29(2):599–609, 2012.

Busse, A., Lützner, M., and Sandham, N. D. "Direct numerical simulation of turbulent flow over a rough surface based on a surface scan". Comput. Fluids, 116: 129–147, 2015.

Cassie, A. B. D. and Baxter, S. "Wettability of porous surfaces". Trans. Faraday Soc., 40:546–551, 1944.

Chang III, Peter A., Piomelli, U., and Blake, W. K. "Relationship between wall pressure and velocity-field sources". Physics of Fluids, 11(11):3434–3448, 1999.

Cheng, H. and Castro, I. P. "Near wall flow over urban-like roughness". Boundary-Layer Meteorology, 104(2):229–259, 2002.

Coceal, O., Thomas, T. G., and Belcher, S. E. "Spatial variability of flow statistics within regular building arrays". Boundary-Layer Meteorology, 125 (3):537–552, 2007.

Farabee, T. M. and Casarella, M. J. "Spectral features of wall pressure fluctuations beneath turbulent boundary layers". Physics of Fluids A: Fluid Dynamics, 3(10): 2410–2420, 1991.

Flack, K. A., Schultz, M. P., and Barros, J. M. "Skin friction measurements of systematically-varied roughness: Probing the role of roughness amplitude and skewness". Flow Turbul. Combust., pages 1–13, 2019.

Forooghi, P., Stroh, A., Schlatter, P., and Frohnapfel, B. "Direct numerical simulation of flow over dissimilar, randomly distributed roughness elements: A systematic study on the effect of surface morphology on turbulence". Physical Review Fluids, 3(4):044605, 2018.

Hu, Z., Morfey, C. L., and Sandham, N. D. "Wall pressure and shear stress spectra from direct simulations of channel flow". AIAA Journal, 44(7):1541–1549, 2006.

Jelly, T. O. and Busse, A. "Reynolds number dependence of reynolds and dispersive stresses in turbulent channel flow past irregular near-gaussian roughness". International Journal of Heat and Fluid Flow, 80:108485, 2019.

Jiménez, J. "Turbulent flows over rough walls". Annu. Rev. Fluid Mech., 36:173–196, 2004.

Ma, R., Alamé, K., and Mahesh, K. "Direct numerical simulation of turbulent channel flow over random rough surfaces". Journal of Fluid Mechanics, 908:A40, 2021.

Mahesh, K., Constantinescu, G., and Moin, P. "A numerical method for large-eddy simulation in complex geometries". Journal of Computational Physics, 197(1):215–240, 2004.

Muppidi, S. and Mahesh, K. "Direct numerical simulations of roughness-induced transition in supersonic boundary layers". Journal of Fluid Mechanics, 693:28–56, 2012.

Panton, R. L., Lee, M., and Moser, R. D. "Correlation of pressure fluctuations in turbulent wall layers". Physical Review Fluids, 2(9):094604, 2017.

Raupach, M. R. and Shaw, R. H. "Averaging procedures for flow within vegetation canopies". Boundary-Layer Meteorology, 22(1):79–90, 1982.

Wenzel, R. N. "Resistance of solid surfaces to wetting by water". Ind. Eng. Chem., 28(8):988–994, 1936.

Yuan, J. and Jouybari, M. A. "Topographical effects of roughness on turbulence statistics in roughness sublayer". Physical Review Fluids, 3(11):114603, 2018.

DISCUSSION

Karen A. Flack, Office of Naval Research

This study highlights the importance of Direct Numerical Simulations over complex rough walls to provide detailed turbulence results within the roughness canopy. The authors are commended on their thorough analysis and innovative techniques to study rough wall boundary layers.

1. Many roughness studies have identified the reduction (and destruction for fully rough flows) of the near-wall peak of the streamwise Reynolds stress. Is this balanced by the increase of dispersive stresses near the wall? Do you anticipate that the magnitude of the peak of the dispersive stress to increase with increased Reynolds number and then plateau for fully-rough conditions?

2. The near-wall results also indicate that surface protrusions enhance pressure fluctuations. Is this strictly a result of flow separation from the roughness feature? Are a few sharp features contributing a large percentage of the increase in form drag?

3. An energy minimization technique is used to solve for the equilibrium positions of liquid-air interfaces over rough surfaces. The technique is demonstrated over a range of surface geometries. Can the methodology / results give insight to flow filling of surface depression with a resulting slip velocity for flows without an interface?

AUTHOR'S REPLY

We thank the referee for helping us further improve the manuscript. We have revised the discussions according to the referee's comments. Our itemized responses to the referee's comments follow.

Question 1: From our results, the reduction of the peak of the streamwise Reynolds stress is not equivalent to the increase of dispersive stresses for both the magnitude and location. It is hard to say that there is a direct correlation between these two quantities. We have performed higher Re_τ cases for the same rough surface (Ma et al., 2021), the results show that the peak of the dispersive stress increases with increased Reynolds number for the transitionally-rough conditions. For the fully-rough regime, further investigation is needed.

Question 2: To further investigate how the pressure fluctuations are increased in the rough-wall flows, we examine the contribution of two dominant Poisson's equation source terms to the fluctuating pressure. Please see the section of rough-wall pressure fluctuations. It is found that the shear layer along with the "roll-up" motion is generated at the upstream stagnation point of the protrusion, and is a primary source of the larger pressure fluctuations. Meanwhile, the dominant slow term shows that the pressure fluctuations are also increased in the regions where the streamwise vortices and the secondary vortices occur, e.g., the region in front of the protrusion and the valley region. The more intense pressure fluctuations are not only due to the roll-up of the attached shear layer, but also the vortical motions and secondary flow interactions within the roughness layer.

We have computed the form drag in two regions separately: one is the 'peak' region above the mean roughness height, the other is the 'valley' region below the mean height. The results show that the form drag in the 'peak' region contributes 73.8% of the total form drag. This suggests that the peaky structures of the rough surface contribute a large percentage of the form drag.

Question 3: Since there is no flow field except for an external pressure, it is not apparent if there is a direct correlation between slip velocity and flow filling. However, one possibility can be through correlating existing slip models with the gas fraction obtained from the equilibrium solution. For different external pressures there is a corresponding equilibrium distribution which results in a specific gas fraction, each value of gas fraction gives a different slip velocity, ranging from a Cassie state to a Wenzel state. The Wenzel state corresponds to the flow filling surface depressions which will have an associated slip velocity with it.